A 4 × 4 Millimeterwave-Frequency Butler Matrix in Grounded Co-Planar Waveguide Technology for Compact Integration With 5G Antenna Arrays

Laura Van Messem, *Student Member, IEEE*, Arno Moerman, *Student Member, IEEE*, Olivier Caytan, *Member, IEEE*, Igor Lima de Paula, Bram Hoflack, Bram Stroobandt, Sam Lemey, *Member, IEEE*, Marc Moeneclaey, *Fellow, IEEE*, and Hendrik Rogier, *Senior Member, IEEE*

***Abstract*— This article presents a novel 4 × 4 Butler matrix implemented in the grounded co-planar waveguide (GCPW) technology, compactly integrated with a highly efficient and broadband 1 × 4 air-filled substrate integrated waveguide (AFSIW) cavity-backed patch antenna array (AA), giving rise to a broad operational frequency range [23.75, 31 GHz] (26.5%) covering the n257, n258, and n261 fifth-generation (5G) bands. Three novel quadrature hybrid couplers and two crossovers are designed and compared to obtain the optimal building blocks for the Butler matrix. Within each of the supported 5G bands, the measured excess insertion loss of the optimized Butler matrix remains smaller than 3.5 dB with a maximal amplitude imbalance of ±0.9 dB. Isolation between input ports is higher than 16.4 dB. A maximal measured realized gain of 12.3 dBi is obtained for the Butler matrix with integrated 1 × 4 AA while ensuring a −3-dB beamwidth coverage of 110°. The main beamsteering directions of [−40°, −14°, 14°, 40°] exhibit measured deviations that stay within ±3°. The fabricated Butler matrix with AA features a very compact footprint of 21.4 mm × 46.0 mm × 2 mm [$2\lambda_0 \times 4.3\lambda_0 \times 0.2\lambda_0$].**

***Index Terms*— Beamforming, Butler matrix, crossover, fifth generation (5G), grounded co-planar waveguide (GCPW), hybrid coupler, millimeterwave (mmWave), multilayer printed circuit board (PCB), size, weight, power, and cost (SWaP-C).**

Manuscript received January 21, 2022; revised April 25, 2022; accepted May 11, 2022. This work was supported in part by the Flemish FWO Research (Advanced multi-antenna communications in the radiative near-field through hybrid focusing and spatial multiplexing) under Project G014719N, in part by the Methusalem funding of the Flemish Government under Grant "SHAPE: Next Generation Wireless Networks," and in part by the European Research Council through "ATTO: A new concept for ultrahigh capacity wireless networks" under Grant 695495. This paper is an expanded version from the IEEE MTT-S International Microwave Workshop Series on Advanced Materials and Processes for RF and THz Applications (IMWS-AMP 2021), Chongqing, China, November 15–17, 2021 [DOI: 10.1109/IMWS-AMP53428.2021.9644020]. *(Corresponding author: Laura Van Messem.)*

Laura Van Messem, Arno Moerman, Olivier Caytan, Igor Lima de Paula, Bram Hoflack, Bram Stroobandt, Sam Lemey, and Hendrik Rogier are with the IDLab-Electromagnetics Group, Department of Information Technology, Ghent University/imec, 9052 Ghent, Belgium (e-mail: laura.vanmessem@ugent.be; arno.moerman@ugent.be; olivier.caytan@ugent.be; igor.limadepaula@ugent.be; bram.hoflack@ugent.be; bram.stroobandt@ugent.be; sam.lemey@ugent.be; hendrik.rogier@ugent.be).

Marc Moeneclaey is with the Department of Telecommunications and Information Processing, Ghent University, 9000 Ghent, Belgium (e-mail: marc.moeneclaey@ugent.be).

Color versions of one or more figures in this article are available at https://doi.org/10.1109/TMTT.2022.3178073.

Digital Object Identifier 10.1109/TMTT.2022.3178073

I. Introduction

THE new generation communication systems aim to expand connectivity, offering 4K video streaming and augmented reality (AR) / virtual reality (VR), introducing self-driving cars and device-to-device (D2D) communication, and connecting smart objects, homes, buildings, and cities to the wireless network [1], [2]. To this end, an increased operational bandwidth is essential [3], still available at millimeterwave (mmWave) frequencies. The resulting increase in path loss can be overcome by employing highly directive antenna arrays (AAs), although this necessitates advanced beamsteering networks. The ecological challenge in this fifth-generation (5G) revolution requires energy-efficient designs [4] while maintaining a small footprint to counter material spill, feasible by minimizing interconnection losses in the feed network and employing antennas with high total efficiency. Exploiting a Butler matrix beamsteering network [5], [6] enables a passive multibeam solution without any additional control signal requirements usually needed by active beamforming chips. In contrast to alternatives, such as Blass and Nolen matrices [7]–[10], it is a cost-effective option and relatively simple to implement due to its modularity, provided by a discrete amount of building blocks. In addition, it can be leveraged in the analog stage of a hybrid beamformer for efficient multi-user mmWave multiple-input multiple-output (MIMO) communication [11]. A judicious selection of the feed network implementation technology is key in achieving a well-balanced trade-off between all figures of merit.

Substrate integrated waveguide (SIW) and air-filled SIW (AFSIW)-based Butler matrix topologies proposed in the literature exhibit significant footprints, complicate compact integration with antennas other than slot arrays, and require dedicated transitions to connect to integrated circuits (ICs) [12]–[19]. In contrast, Butler matrix implementations based on stripline (SL), microstrip line (MSL), and co-planar waveguide (CPW), which are often integrated with simple, yet less efficient, patch AAs, have an increased transmission loss [20] and the spurious radiation of the routing network influences the radiation pattern of the AA [21]–[28].

This article presents a novel compact 4 × 4 Butler matrix in the grounded CPW (GCPW) technology, for direct integration

TABLE I
COMPARISON OF THE PROPOSED SOLUTION WITH THE STATE-OF-THE-ART DESIGNS

Ref.*	Δf_0(GHz)	FBW(%)	η(%)	FP($\lambda_0 \times \lambda_0$)	h(mm)	ε_r , tan δ	PG(dBi)	SLL(dB)	Cov.(°)	IL(dB)	AI(dB)	I(dB)	Technology
[12]	[28, 32]	13.3	N/A	4.2×11	N/A	2.2, 0.0009	12	-10	122	0.3^+	1.2^+	6	1L, SIW, 2×4 slot
[13]	[28, 32]	13.3	N/A	2.7×7.2	0.508	2.2, 0.0009	12.1	-10	140	1	5.6	10	1L, SIW, 2×4 slot
[14]	[28, 31]	10	N/A	4×10	1.016	2.2, 0.0009	15**	-10**	110	2	N/A	7	M1L, SIW, 2×8 slot
[15]	[28.5, 31.5]	10	N/A	19.4×23.5	1.1^+	2.2, 0.0009	13	-8**	130	N/A	N/A	11.5	M1L, SIW, 2×8 slot
[16]	[32, 43]	29.3	48.3	$17\times26^+$	3	2.2, 0.0009	12.8 dBic	-6**	76	N/A	N/A	20	M1L, SIW, 1×4 array
[17]	[27, 29]	7.1	N/A	$4.5\times10^+$	1.524	2.2, 0.0009	12.4	-8**	2D	N/A	N/A	15	M1L, SIW, 3×3 slot
[18]	[51.5, 70.5]	31.1	64‡	4.2×5.1	1.27	2.94, 0.0012	12.4	-9	2D	1.3	1.2	15	M1L, SIW, 2×2 patch
[19]	[9.5, 10.5]	10	24	16.7×22	1	2.55, 0.001	12.1	-7**	2D	6**	7**	10	1L, SIW, 4×4 patch
[21]	[27.5, 28.5]	3.6	55	4.6x5.6	0.254	2.2, 0.0009	10.7	-11**	90	1.7^+	5^+	15	ML, MSL, 1×6 dipole
[22]	[26, 31.4]	19	29	6.7×11.5	1.62	2.9, 0.0025	12	-8	84	4	N/A	15	ML, MSL, 4×4 patch
[23]	[25.2, 29.6]	15.7	N/A	3.5×4.7	6.2	3/4, 0.0014	6.7	-5.3	100**	2.9	N/A	N/A	1L, MSL, 1×4 patch
[24]	[26.5, 29.5]	10.7	N/A	$2.2\times4.2^+$	0.508	3.55, 0.0027	N/A	-5**	100**	5	7	N/A	1L, MSL, 1×4 patch
[25]	[5.5, 6.3]	13.6	N/A	2.2×2.73	0.254	3, 0.001	N/A	-3**	240	1^+	2^+	N/A	1L, MSL, 1×4 array
[26]	[5, 6.5]	10.3	N/A	$2\times3^+$	1.27	10.2, 0.0023	N/A	-5**	N/A	1.5	7**	10	1L, CPW, 1×4 patch
[27]	[2.5, 3.5]	33.3	N/A	1×1.3	3.2	3.38, 0.0025	N/A	N/A	N/A	1	0.9	25	ML, SL
[28]	[24.5, 26.5]	11.8	N/A	2.9×3	2.674	4.4/2.2	11**	-5**	100**	1.1	1.1	11	M1L, SISL, 2×4 patch
[29]	[89, 97]	0.7	N/A	31×50	3.9	1, -	N/A	N/A	N/A	1	3	23	SLA printed RWG
[30]	[21.8, 22.3]	2.3	N/A	2.9×2.9	1.47^+	1, -	11.2	-7**	2D	0.6	0.25	10	RWG, 2×2 array
This paper	**[26.5, 29.5]**	**10.7**	**55⁺**	**2×4.3**	**2.042**	**3.66, 0.0037**	**12.3**	**-8.3**	**110**	**3.4**	**1.8**	**16.6**	**M1L, GCPW, cavity**
	[24.25, 27.5]	**12.6**					**11.3**	**-7**	**117**	**3.5**	**1.7**	**16.4**	
	[23.75, 31]	**26.5**					**12.3**	**-6**	**95**	**3.8**	**2.2**	**16.4**	

* Δf_0 = frequency range, FBW = fractional bandwidth, η = total efficiency, FP = footprint, h = height, ε_r = relative permittivity, tan δ = loss tangent, PG = peak gain, SLL = side lobe level, IL = average excess insertion loss, AI = amplitude imbalance, I = isolation, Cov. = 3-dB beamwidth coverage, 1L = single-layer PCB, M1L = stacked 1Ls, ML = multi-layer PCB, (SI)SL = (suspended integrated) stripline, SLA = stereolithography, RWG = rectangular waveguide, ‡ = reduced range [55, 66] GHz, $^+$ = derived from simulated curves, ** = derived from measured curves.

with a highly efficient, broadband 1 × 4 AFSIW cavity-backed patch AA [31] to obtain a total solution with favorable size, weight, power, and cost (SWaP-C), covering all global 5G 26- and 28-GHz bands, being: n257 [26.5, 29.5] GHz, n258 [24.25, 27.5] GHz, and n261 [27.5, 28.35] GHz while facilitating integration with additional communication ICs. To the best of the authors' knowledge, neither the components nor a full mmWave GCPW Butler matrix manufactured in standard printed circuit board (PCB) technology have yet been pursued. This article substantially extends the conference paper [32] by proposing three novel implementations of quadrature hybrid couplers and two novel crossover designs in the GCPW technology. The Butler matrix, incorporating the best performing building blocks and occupying a compact footprint of only 19.2 mm × 29.9 mm × 0.65 mm, allows easy integration with antenna topologies employing a GCPW feed, (M)SL via tapering, and (AF)SIW technology via slot coupling. The latter is demonstrated by compactly integrating the Butler matrix with four broadband and highly efficient AFSIW cavity-backed patch antennas in an array configuration, as presented in [31], and by fully validating the integrated solution in the entire [23.75, 31] GHz frequency band.

Table I provides an overview of the state-of-the-art Butler matrix implementations, including the design proposed in this work. Note the compact footprint of the proposed solution while maintaining broadband operation. The average excess insertion loss of 3.5 dB is better than most proposed MSL implementations. The isolation (>16.4 dB in case of the standalone Butler matrix and >10.4 dB after integration with the AA) competes with (AF)SIW solutions. Considering the four antenna element layout, our design achieves a high measured gain amounting up to 12.3 dBi, with an excellent −3-dB beamwidth coverage of 110° for all 5G bands.

Section II gives an overview of the proposed system and details the design, integration, and fabrication requirements. Section III compares three different GCPW implementations of quadrature hybrid couplers, as well as two different crossover designs. The optimal building blocks are assembled in a 4 × 4 Butler matrix and the performance is evaluated in Section IV. The beamsteering capabilities with integrated 1 × 4 AFSIW cavity-backed patch AA are demonstrated in Section V, whereas Section VI elaborately compares our solution to the state of the art. A conclusion is formulated in Section VII.

II. BUTLER MATRIX TOPOLOGY

Before providing a detailed description of the design procedure for the Butler matrix, we first outline its overall architecture, being a composition of hybrid couplers, crossovers, and phase shifters implemented in the GCPW technology. Then, we list the different specifications we target during the design process. Next, we discuss the requirements imposed on the Butler matrix to optimally interface with the 1 × 4 AFSIW AA proposed in [31].

A. System Overview

Fig. 1 shows the architecture of the proposed Butler matrix with compactly integrated AA. The Butler matrix consists of four quadrature hybrid couplers, two crossovers, and two phase shifters to support four beams. The quadrature hybrid couplers provide near 3-dB power splitting while maintaining a stable 90° phase difference between their output ports and are designed for minimum insertion loss and amplitude/phase imbalance. Fixing the two phase shifters and crossovers yields the required phase difference between adjacent antenna elements δ such that each input port excitation of the Butler matrix (ports 1–4) gives rise to a distinct main beam direction θ [33], as shown in Fig. 1. The Butler matrix is directly integrated at the backside of the broadband and highly efficient 1 × 4 uniform linear array (ULA) proposed in [31],

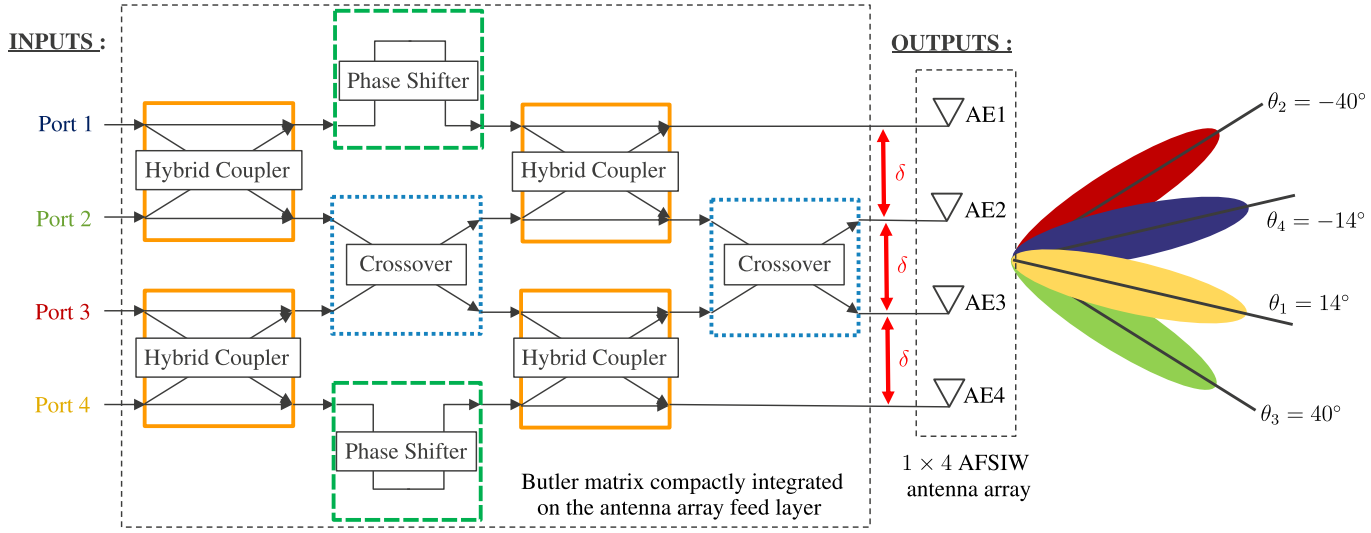

Fig. 1. Block diagram of the proposed Butler matrix with integrated AA.

which is implemented in the stacked AFSIW PCB technology. This approach ensures peak performance in a compact footprint by minimizing the interconnect lengths and reusing the AA as an integration platform.

B. Specifications

Both the standalone Butler matrix and the Butler matrix with integrated 1 × 4 array are designed for efficient and robust operation in all worldwide-planned 26- and 28-GHz 5G bands, being the n257 [26.5, 29.5] GHz, the n258 [24.25, 27.5] GHz, and the n261 band [27.5, 28.35] GHz. Thereto, all input and output reflection coefficients with respect to 50 Ω should remain below −10 dB in the entire [23.75, 31] GHz band, including a 2-GHz impedance bandwidth margin to mitigate detrimental effects from fabrication process variations. Hence, a large fractional bandwidth of 26.5% is pursued. In addition, in each of the supported 5G bands, the Butler matrix is designed to ensure a peak realized gain above 10 dBi, a sidelobe level (SLL) below −6 dB, a port-to-port isolation of at least 10 dB, and simultaneous support of four distinct beams in the azimuth plane with main beam directions (θ) [−40°, −14°, 14°, 40°] and a θ-deviation not exceeding 5°. The latter is chosen to ensure a total −3-dB beamwidth system coverage of more than 90° while not exceeding the −3-dB beamwidth of the single antenna element [31]. Table II lists for each input port excitation the main beam direction θ and the required phase difference between adjacent antenna elements δ. The derived target specifications for the individual components are listed in Section III.

C. Integration Requirements

The 1 × 4 AFSIW AA is realized by stacking three low-cost single-layer PCB laminates: a 0.254-mm-thick RO4350B substrate for the GCPW feed of the antenna elements, a 1-mm-thick FR-4 layer to implement air-filled edge-plated cavities, and another 0.254-mm-thick RO4350B substrate for the radiating antenna patches on top [31]. The proposed Butler matrix is implemented on the same layer as the GCPW feed lines of the antenna, capitalizing on the excellent antenna-to-platform isolation offered by the antenna topology and reducing feed

TABLE II

PHASE DIFFERENCE BETWEEN ADJACENT PORTS δ AND SIMULATED MAIN BEAM DIRECTION θ FOR EACH INPUT PORT EXCITATION

	Port 1	Port 2	Port 3	Port 4
δ	−45°	135°	−135°	45°
θ	−14°	40°	−40°	14°

line losses to the bare minimum. An additional 0.254-mm-thick RO4350B substrate is used at the bottom of the stack to implement a multilayer crossover. Considering all 35-μm-thick conductor layers, this results in a total thickness of 2.042 mm for the Butler matrix with integrated AA.

III. PASSIVE BUILDING BLOCKS

This section elaborately discusses and compares novel implementations of the passive building blocks that are needed for a GCPW-based Butler matrix. Standard PCB manufacturing is adopted for the fabrication of all prototypes. Measurements of the prototypes, using SouthWest 2.4-mm female end launch press-fit connectors, are performed with a Keysight N5247B PNA-X vector network analyzer (VNA).

A. Quadrature Hybrid Coupler Designs

Three distinct designs, implemented in the GCPW technology for minimal insertion loss and decent power handling, are shown in Fig. 2. The optimized behavior of the double branch-line and triple branch-line hybrid couplers is shown in Fig. 3(a) and (b), respectively. The two latter designs are used for benchmarking. The best performing design is the novel bent quadrature hybrid coupler in Fig. 2(c), of which the optimized behavior is plotted in Fig. 3(c). By bending the classic square topology [34], fabrication difficulties concerning the required copper pad around each via for full GCPW realization are mitigated, thereby enabling scaling to even higher frequencies. The employed PCB manufacturer's guidelines dictate a copper clearance of at least 0.1 mm. Furthermore, signals can easily be routed to the hybrid coupler under any incoming angle because of the bent feed lines. This allows the efficient and compact integration of the beamforming network with

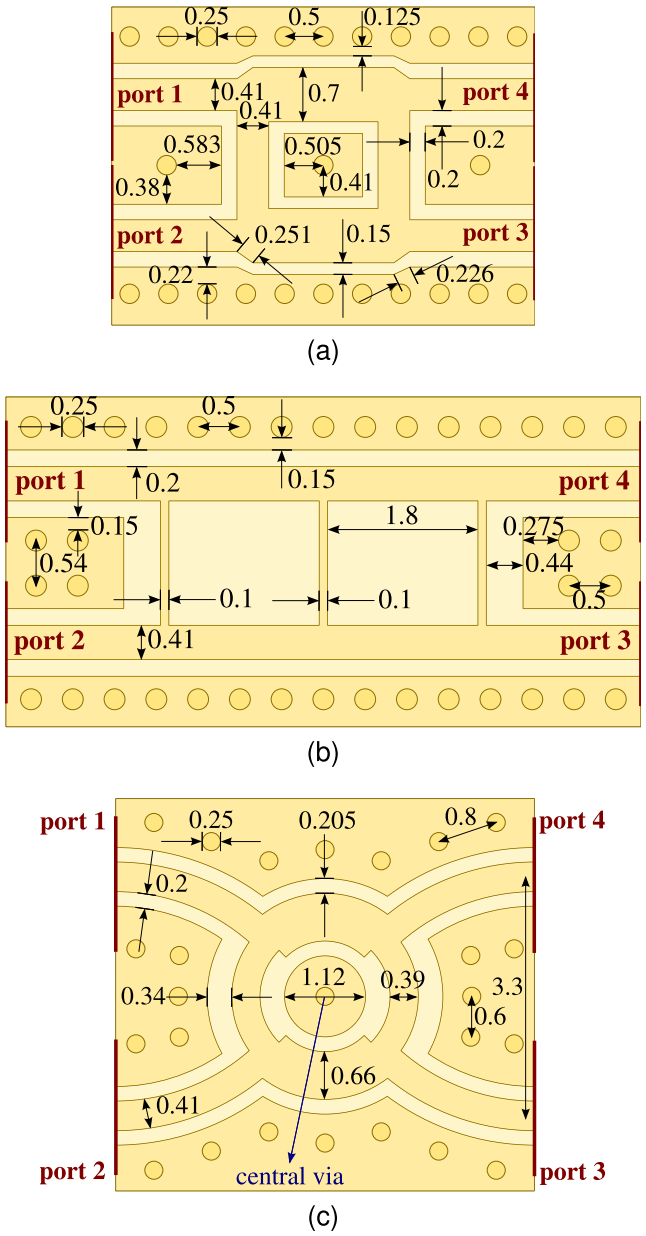

Fig. 2. Quadrature hybrid coupler design layout with annotated dimensions in millimeter. (a) Double branch-line coupler in a footprint of 4.1 mm × 5.5 mm. (b) Triple branch-line coupler in a footprint of 4.0 mm × 7.6 mm. (c) Bent hybrid coupler design in a footprint of 5.2 mm × 5.5 mm.

active electronic and even opto-electronic components [35], [36] into an antenna unit.

1) Specifications: Optimization of the designs targets multiple requirements, such as keeping the excess insertion loss below 1 dB as well as ensuring an amplitude imbalance below 0.5 dB. A return loss above 10 dB and an isolation higher than 15 dB are aimed for while retaining a stable phase difference between the output ports close to 90°, where the imbalance remains within 5°.

2) Design: To simplify the design procedure of the bent topology, the sum of the trace width and twice the gap width is kept constant in the circular part of the design [see Fig. 2(c)]. In particular, the final dimension amounts to $0.39+2\times0.34 = 0.66+2\times0.205 = 1.07$ mm. Similar to the design procedure of a classic square branch-line coupler, the impedances of the transmission lines (TMLs) are initially set to $Z_{0,i} = 50\,\Omega$ and $Z_{0,i}/\sqrt{2} = 35.4\,\Omega$ [37]. Full-wave optimization using CST Microwave Studio results in characteristic impedances of $Z_{0,\mathrm{opt}} = 55\,\Omega$ and $Z_{0,\mathrm{opt}}/\sqrt{2} = 38.9\,\Omega$ for the TMLs of the bent hybrid coupler design when optimizing for minimal insertion loss. The incoming GCPW feed traces are still matched to 50 Ω to minimize reflections. Adding the central via [see Fig. 2(a) and (c)] is essential for a full GCPW realization. Notice that how the triple branch-line coupler in Fig. 2(b) has its middle section implemented in (quasi-) MSL, to achieve a nominal impedance of $Z_{1,i} = (\sqrt{2}+1)Z_{0,i} = 120.7\,\Omega$ [38]. The required dimensions to realize this impedance in the GCPW technology exceeds the space available within the GCPW sections on the top and bottom, and the manufacturing capabilities.

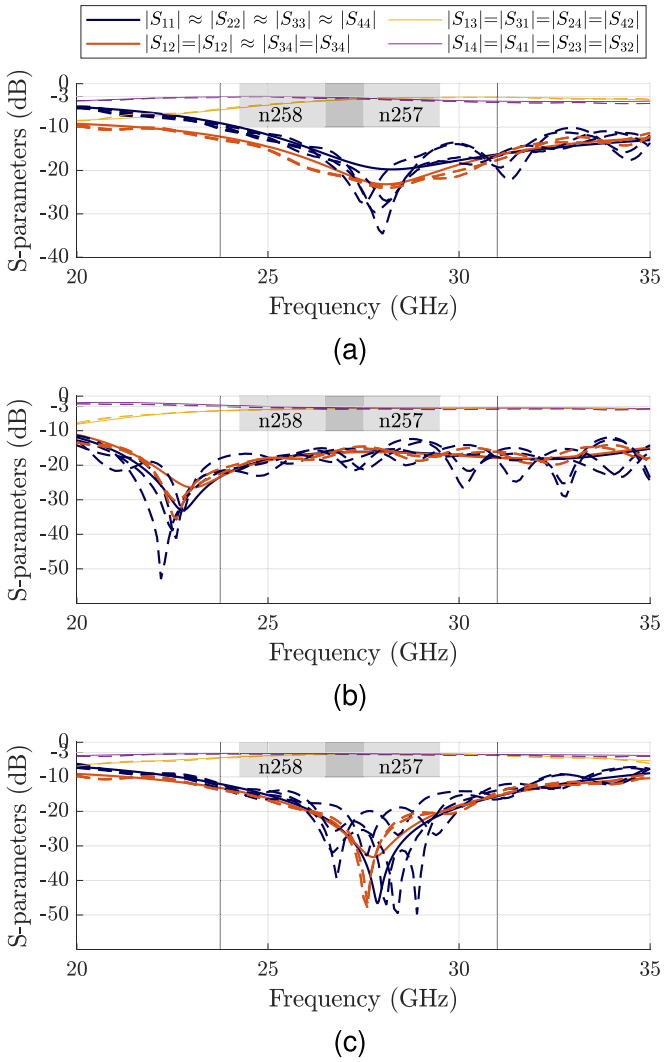

Fig. 3. Measured (dashed) and simulated (solid) scattering parameters of all quadrature hybrid couplers. (a) Double branch-line coupler. (b) Triple branch-line coupler. (c) Bent hybrid coupler.

3) Performance: The fabricated prototypes are shown in Fig. 4. The measurements are performed after thru-reflect-line (TRL) calibration up to the port planes defined in Fig. 2. The measured and the simulated behavior of all quadrature hybrid coupler designs, which are plotted in Fig. 3, agree well and show that the bent hybrid coupler exhibits the lowest reflection coefficients (blue curves) and the highest isolation toward undesired ports (red curves), while the double

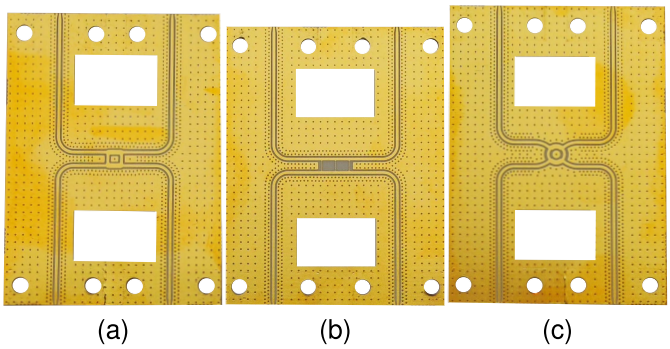

Fig. 4. Pictures of the quadrature hybrid coupler prototypes. (a) Double branch-line coupler. (b) Triple branch-line coupler. (c) Bent hybrid coupler.

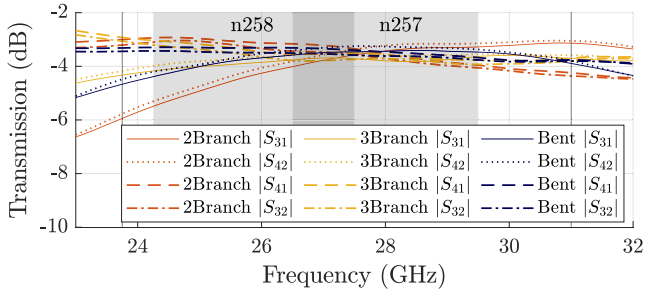

Fig. 5. Measured transmission characteristics of all couplers.

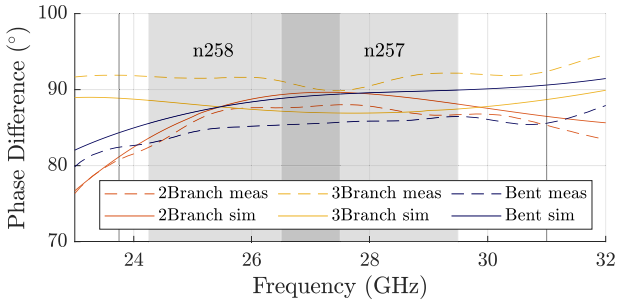

Fig. 6. Measured (dashed) and simulated (solid) output port phase difference of all quadrature hybrid coupler designs.

TABLE III
OVERALL WORST-CASE MEASURED (SIMULATED) PERFORMANCE FOR ALL PASSIVE BUILDING BLOCKS

[26.5, 29.5] GHz*	IL (dB)	AI (dB)	RL (dB)	I (dB)	PI (°)
Double branch	1.2 (0.9)	1 (0.8)	14.4 (16.1)	20.5 (18.8)	1.4 (1.6)
Triple branch	0.9 (0.7)	0.5 (0.4)	12.4 (16.1)	14.6 (16.2)	2.3 (0.6)
Bent hybrid	0.8 (0.5)	0.5 (0.2)	14.8 (21)	20 (20.1)	1.1 (1.2)
Bent crossover	1.1 (0.5)	0.5 (0.1)	17.1 (20.3)	15.1 (16.3)	0.4 (0.1)
Multi-layer	0.5 (0.4)	0.2 (0.1)	15.3 (17.7)	43.2 (39.2)	4 (3.3)

* IL = excess insertion loss, AI = amplitude imbalance, RL = return loss, I = isolation, PI = phase imbalance.

branch-line coupler shows the highest transmission loss and largest amplitude imbalance (purple and yellow curves) over the frequency range [24.25, 29.5] GHz. The latter can also be seen in Fig. 5, showing an enlarged version of the measured transmission characteristics of all hybrid couplers. Notice that some manufacturing tolerances introduce a slight asymmetry in the fabricated prototypes since we notice small differences between $|S_{31}|$ and $|S_{41}|$, and between $|S_{32}|$ and $|S_{42}|$. The comparison between the measured and simulated phase relations of both output ports, being $(\angle S_{31} - \angle S_{41})$, is presented in Fig. 6. The full GCPW realization of the bent hybrid coupler shows reliable phase behavior, with a small measured phase imbalance of $\pm 0.55°$ over the n257 band and $\pm 1.2°$ over all 5G bands [24.25, 29.5] GHz.

Numerical comparison of the performance of all three designs in the n257 band is presented in Table III. The bent hybrid coupler achieves the best measured results in terms of excess insertion loss (<0.8 dB) and amplitude imbalance (<0.5 dB), fulfilling the aforementioned proposed specifications. The bent hybrid coupler also performs best in terms of return loss (>14.8 dB) and phase imbalance (<1.1°). The achieved performance meets the requirements for return loss and phase imbalance by a large margin. In terms of isolation, we see that the bent hybrid competes with the double branch-line coupler (>20 dB), both achieving much better isolation than the targeted 15 dB. Similar observations can be made in the n258 and n261 bands. The footprint of the double branch-line coupler equals 4.1 mm × 5.5 mm = 22.55 mm^2, compared to 4.0 mm × 7.6 mm = 30.4 mm^2 for the triple branch-line coupler and 5.2 mm × 5.5 mm = 28.6 mm^2 for the bent hybrid design.

4) Conclusion: Considering all figures of merit, we conclude that the novel bent hybrid coupler, fully implemented in GCPW technology, performs best. This design enables easy integration into a full Butler matrix due to its bent input and output signal lines while ensuring low radiation losses and a compact footprint.

B. Crossover Designs

Fig. 7 shows the two proposed crossover topologies in the GCPW technology. Traditional crossover designs are usually realized by concatenating two quadrature hybrid couplers, typically resulting in a bulky and lossy crossover component. The bent hybrid coupler-based crossover shown in Fig. 7(a) serves as a benchmark. Its optimized performance is shown in Fig. 8(a). The novelty of the multilayer crossover, presented in Fig 7(b), lies in its compact GCPW implementation, where the indirect path provides an additional degree of rotational freedom due to the coax-like transition, matched to 50 Ω. Moreover, separating the signal paths provides excellent crosstalk suppression, confirmed by the scattering parameters plotted in Fig. 8(b).

1) Specifications: Optimization of the designs aims for multiple goals, such as keeping the insertion loss below 1 dB as well as ensuring an amplitude imbalance below 0.5 dB. In addition, a return loss above 10 dB and an isolation higher than 15 dB are targeted while minimizing the phase difference between the output ports, keeping the imbalance within 5°.

2) Design: The coax-like transition of the multilayer crossover is matched to 50 Ω to ensure minimal reflection. By applying the impedance calculations in [37], we obtain for the ratio between the outer and inner diameter of the coax: $d_{\text{outer}}/d_{\text{inner}} = 4.93$. Initially, the starting values are set to $d_{\text{inner}} = \text{via}_d = 0.25$ mm and $d_{\text{outer}} = 1.23$ mm, where, given the via implementation of the outer conductor, we expect d_{outer} to increase slightly after optimization to obtain a perfect 50-Ω match, according to [39]. Manufacturing guidelines specify a via pad clearance of 0.25 mm, which results in a total pad diameter of 0.5 mm, as shown in Fig. 7(b).

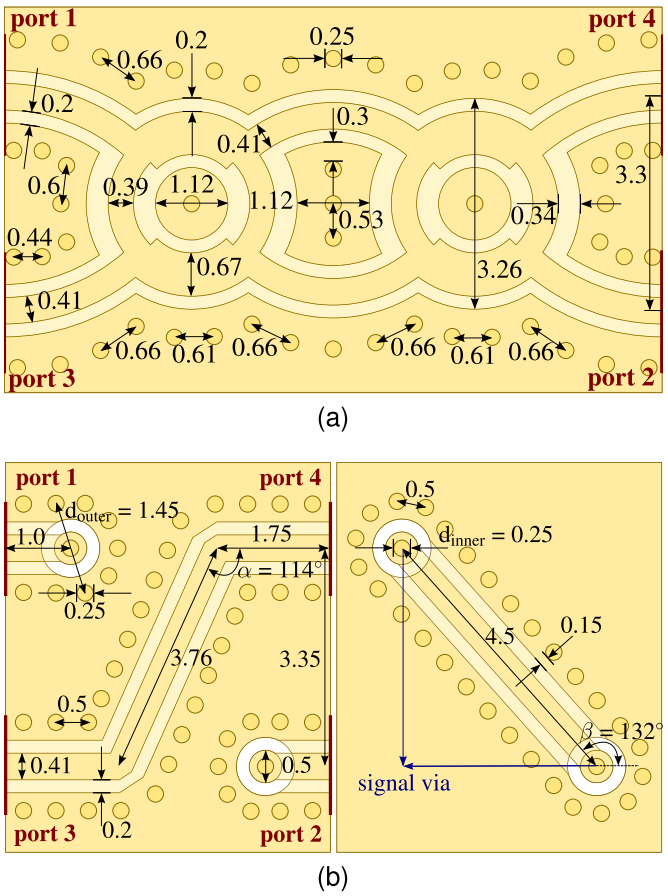

Fig. 7. Crossover topologies with annotated dimensions in millimeter. (a) Bent hybrid coupler-based crossover design in a footprint of 5.5 mm × 10.2 mm. (b) Multilayer crossover in a footprint of 5.0 mm × 5.1 mm: top (left) and bottom (right) copper layer with a copper ground plane layer in the middle to minimize crosstalk.

Since both signal paths of the multilayer crossover are not necessarily of identical electrical length, special attention is devoted to preserving an equal signal phase at the output ports. This can be easily controlled by exploiting the degrees of freedom given by the design angles α and β. The two PCB layers for the multilayer crossover are assembled by adding an appropriate amount of solder paste on the via pads of the signal vias in the middle of the coax-like structure, shown on the right of Fig. 7(b). Both layers are then temporarily fastened with brass screws of 1 mm diameter while applying a heatgun to reflow the solder paste locally. Finally, the screws are removed and the galvanic contact between both PCB layers is verified.

The fabricated multilayer crossover prototype has a small air gap between both PCB substrates due to the etching process and the soldering. Simulations show that a larger air gap increases the phase of the multilayer path from port 1 to port 2: $\angle S_{21}$. To accommodate for the presence of such an air gap, the initially designed phase of the indirect path (port 1 to 2) is 25° smaller than for the direct path (port 3 to 4), giving some leeway to the fabricated prototypes' output port phase difference. An air gap thickness variation from 1 to 5 μm corresponds to an additional phase shift within ±5°. A consistent fabrication technique resulted in an air gap of about 3 μm between both PCBs, corresponding to a phase difference of 20.5° between both output ports at the center

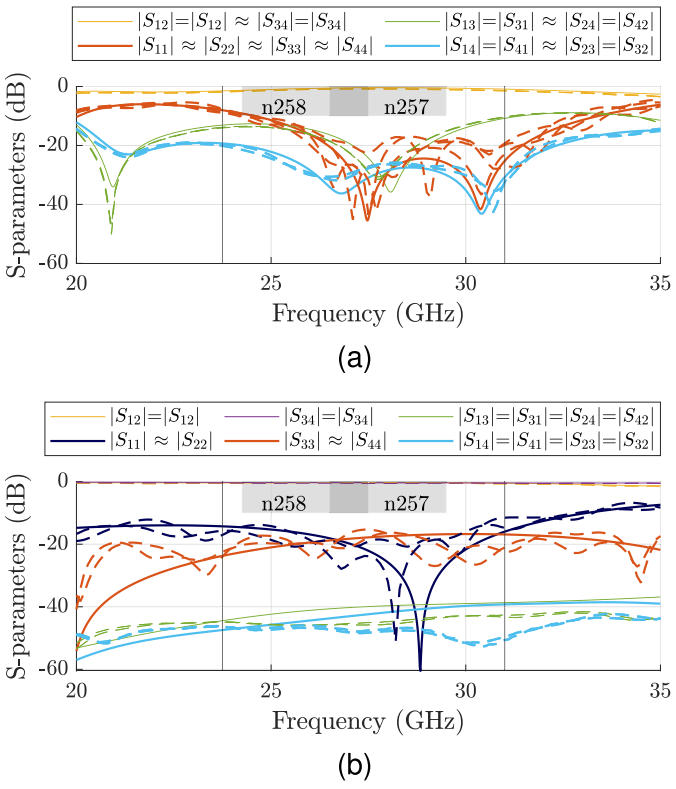

Fig. 8. Measured (dashed) and simulated (solid) scattering parameters of all GCPW crossovers. (a) Bent hybrid coupler-based crossover. (b) Multilayer crossover.

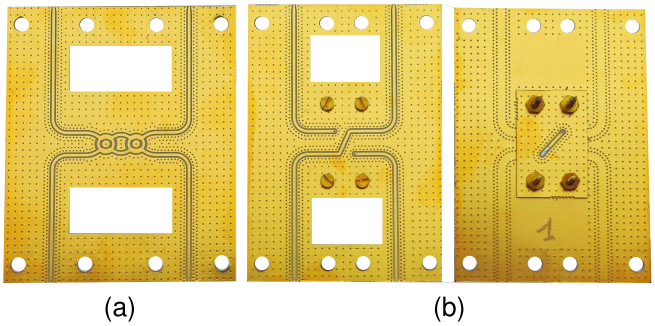

Fig. 9. Pictures of both crossover prototypes. (a) Bent hybrid coupler-based crossover design. (b) Multilayer crossover: top view (left) and bottom view (right).

frequency of 28 GHz, which can be compensated for when designing the full Butler matrix. In terms of magnitude of the transmission coefficient, the influence of an air gap thickness between 1 and 5 μm causes negligible variations smaller than 0.06 dB.

3) Performance: The fabricated prototypes of both crossovers are shown in Fig. 9. All measurements are performed after TRL calibration up to the port planes defined in Fig. 7. The comparison of the measured and simulated behavior of both crossover designs, shown in Fig. 8, proves good agreement and shows that the multilayer crossover exhibits the lowest reflection coefficients, the highest isolation between undesired ports, and the lowest transmission loss over the frequency range [24.25, 29.5] GHz. Fig. 10 shows an enlarged version of the measured transmission characteristics of both crossovers. In case of the concatenated

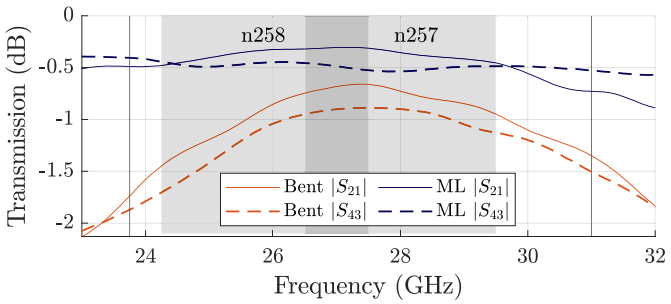

Fig. 10. Measured transmission characteristics of both crossovers.

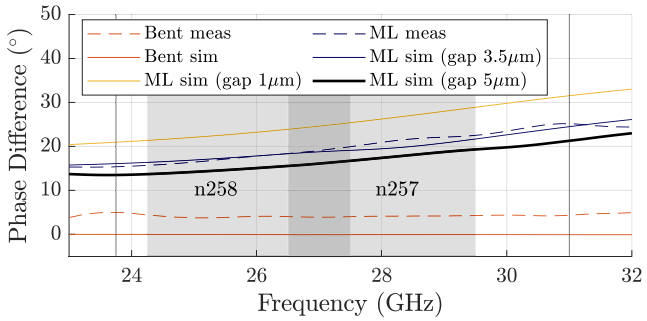

Fig. 11. Measured (dashed) and simulated (solid) output port phase difference of both crossover designs.

bent hybrid coupler-based crossover, the manufacturing tolerances introduce a slight asymmetry in the fabricated prototypes, which is characterized by an amplitude imbalance $||S_{21}| - |S_{43}|| < 0.25$ dB. The amplitude imbalance of the multilayer crossover remains below 0.21 dB at every frequency, which is smaller than its bent crossover alternative. The larger insertion loss and frequency-dependent behavior of the bent crossover make this solution less attractive than the multilayer crossover.

The comparison between the measured and simulated phase relations of both output ports, being $(\angle S_{21} - \angle S_{43})$, is represented in Fig. 11 for both crossover designs. A consistent fabrication technique for the multilayer crossover resulted in an air gap around 3 μm between both PCBs. The phase imbalance remains within ±2.5° in the n257 5G frequency band, for both simulation and measurement, and within ±4.5° for the entire [24.25, 29.5] GHz band.

Numerical comparison of both designs is presented in Table III for the n257 band. From this table, we see that the multilayer crossover achieves the best measured results in terms of insertion loss (<0.5 dB) and amplitude imbalance (<0.2 dB), fulfilling the target specifications on insertion loss (<1 dB) and amplitude imbalance (<0.5 dB). The multilayer crossover also performs best in terms of isolation (>43 dB), which is significantly better than the postulated value of >15 dB. Consequently, the excellent isolation achieved by the multilayer crossover exceeds high-performance SIW implementations [12], [19], [40] while maintaining an extremely compact footprint. In terms of return loss, we see that the multilayer crossover competes with the bent hybrid-based crossover (>15 dB), both satisfying the requirement of 10 dB. The phase imbalance of the multilayer crossover is slightly worse than the benchmark design (<4°).

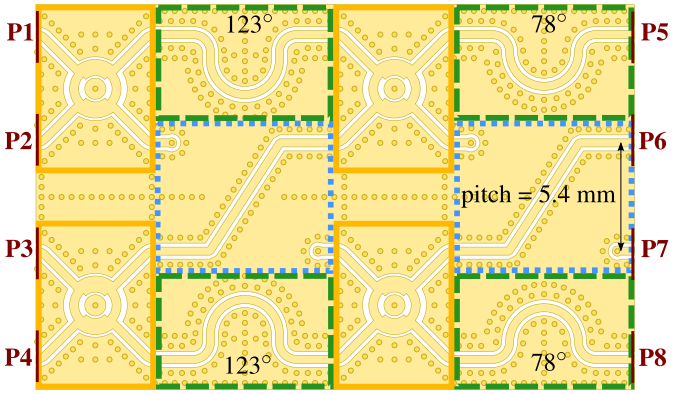

Fig. 12. Full Butler matrix design with highlighted building blocks, color coded according to Fig. 1.

However, this is a trade-off with the substantially improved transmission coefficient and isolation, and it still complies with the targeted limit of 5°. Similar observations can be made in the n258 and n261 bands. In addition, the multilayer crossover is significantly more compact with a footprint of only 5.0 mm × 5.1 mm = 25.5 mm^2, compared to a footprint of 5.5 mm × 10.2 mm = 56.1 mm^2 for the bent hybrid-based crossover, which is more than double.

4) Conclusion: Considering all figures of merit, we conclude that the novel multilayer crossover, fully implemented in GCPW technology, performs best. This design enables a very compact realization of a full Butler matrix, while the rotational degree of freedom of the indirect multilayer path, due to the matched 50-Ω coax-like transition, allows easy manipulation of the phase difference between both output ports by adjusting the rotation angle β, currently set to 132° [see Fig. 7(b)].

IV. Standalone Butler Matrix

The spacing between the GCPW tracks of the best performing bent quadrature hybrid coupler and multilayer crossover, carefully examined in Section III, is adapted to match the antenna pitch of half a wavelength at 29.5 GHz, being 5.4 mm. The full 4 × 4 Butler matrix consists of four bent hybrid couplers, four phase shifters, and two multilayer crossovers, as shown in Fig. 12. It fits within a footprint of 19.2 mm × 29.84 mm × 0.648 mm [$1.8\lambda_0 \times 2.8\lambda_0 \times 0.06\lambda_0$].

A. Phase Shifters

The adapted multilayer crossover with GCPW track pitch of 5.4 mm exhibits a phase shift of $\angle S_{21} = \angle S_{43} = 78°$ for both its signal paths. Consequently, two additional phase shifters of 78° are introduced on top of the two essential 45° phase shifters, to compensate for the additional path length introduced by the crossovers. These can be found at the right edge in Fig. 12. Both 45° phase shifters also get an additional phase shift of 78°, resulting in a total phase of 123°, present at the center-left side of Fig. 12.

B. Measured Results

The measured transmission characteristics of the full eight-port standalone Butler matrix after TRL calibration are

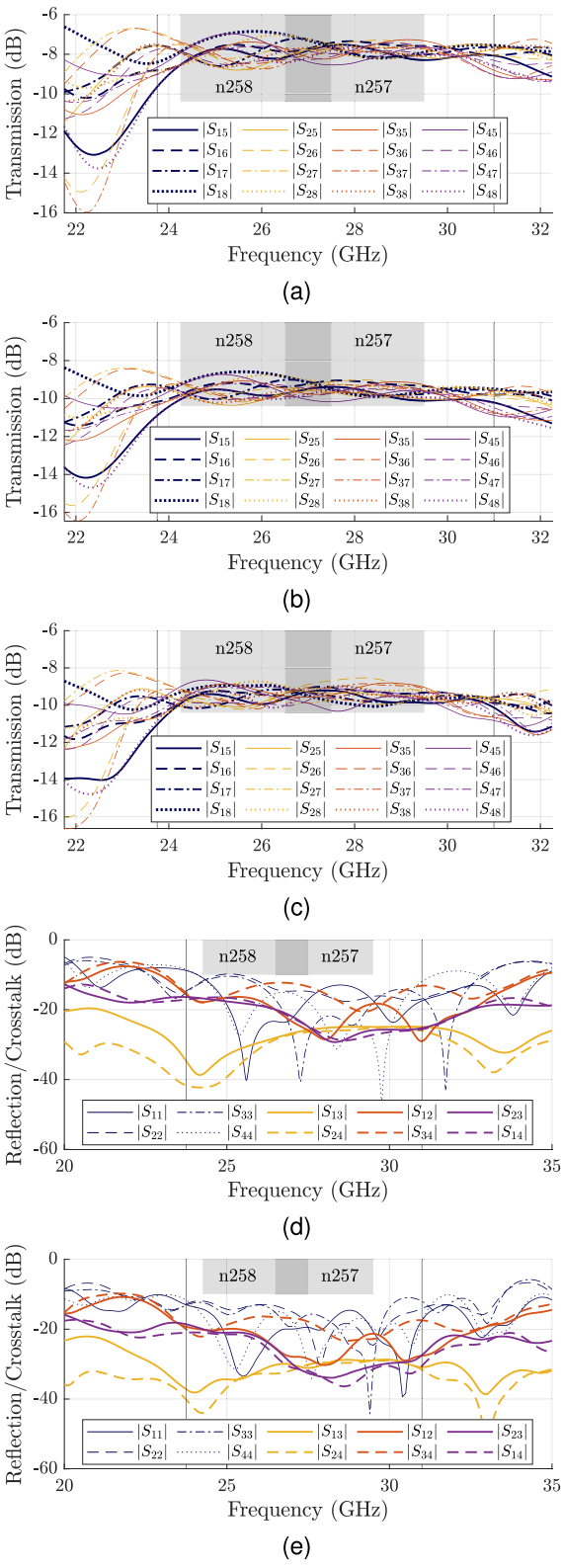

Fig. 13. Standalone Butler matrix, transmission coefficients: simulated (a) without and (b) with surface roughness and ENIG surface finish versus (c) measured, and input reflection coefficients and crosstalk between the input ports: (d) simulated (with surface roughness and ENIG surface finish) versus (e) measured.

shown in Fig. 13(c). The TRL calibration allows de-embedding of the employed SouthWest 2.4-mm female end launch connectors and the longer GCPW tracks, which are essential to ensure that the transition effects from the capacitive connector press have died out. The measured excess insertion loss varies between 2.5 and 4.3 dB for all covered 5G bands. The increased losses are mainly attributed to a high surface roughness value at the side of the laminate ($R_a = 7\,\mu$m) [41] and the ferromagnetic properties of nickel in the electroless nickel/immersion gold (ENIG) surface finish [42], with the covering gold layer being much thinner than its skin depth. This is confirmed by simulation in Fig. 13(a) and (b).

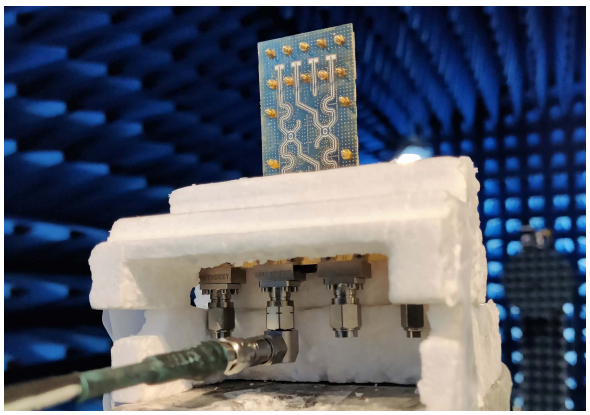

Fig. 14. Butler matrix with integrated 1 × 4 ULA prototype inside the anechoic chamber.

The simulated and measured input reflection coefficients and crosstalk between the input ports of the full eight-port standalone Butler matrix are shown in Fig. 13(d) and (e), respectively. It shows good agreement between simulation and measurement. The measured reflection coefficients stay below −13.3 and −11.9 dB, whereas the isolation is higher than 16.6 and 16.4 dB for the n257 and n258 bands, respectively. In the n261 band, a return loss above 15.7 dB and a crosstalk below −17.8 dB are measured. Similar performance is obtained at the output ports of the Butler matrix. In conclusion, the proposed Butler matrix achieves all corresponding targets provided in Section II.

V. Beamsteering

Finally, the Butler matrix, proposed and validated in Section IV, is compactly integrated with a 1 × 4 ULA, consisting of highly efficient AFSIW cavity-backed patch antennas [31]. The fully integrated prototype, equipped with four press-fit connectors (one for each distinct ULA steering angle), is deployed and characterized inside an anechoic chamber, mimicking free-space conditions. As shown in Fig. 14, the prototype is mounted such that the H-plane, in which the main beam can be steered by selecting the input port, corresponds to the azimuth plane. By means of an NSI-MI spherical measurement system operating in the far-field mode, a Keysight N5242B PNA-X VNA, and an NSI-MI standard gain horn [22, 33] GHz, the far-field gain patterns are characterized in the azimuth plane through the gain comparison method. Each port is measured separately, with the other ports being terminated by 50-Ω loads. The simulated and measured isolation and reflection coefficients of the prototype are shown in Fig. 15(a) and (b), respectively.

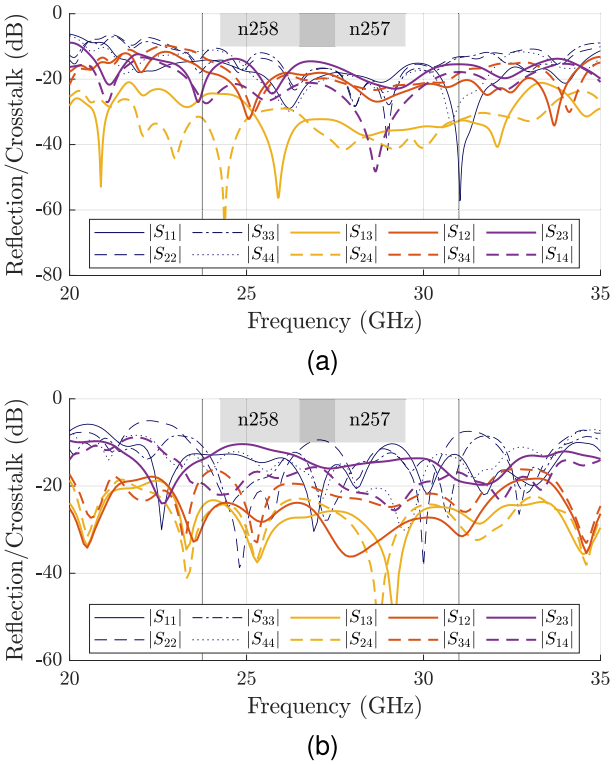

Fig. 15. Full Butler matrix with integrated AA, input reflection coefficients, and crosstalk between input ports: (a) simulated and (b) measured.

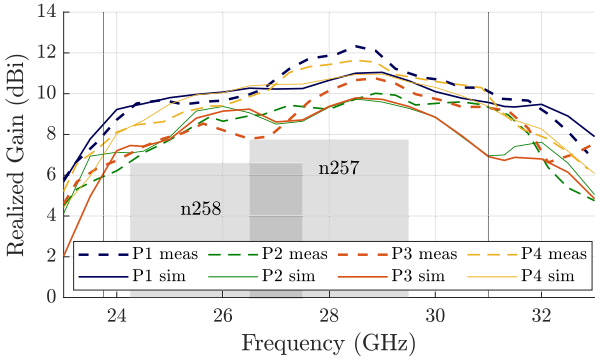

Fig. 16. Measured (dashed) and simulated (solid) realized peak gain in the azimuth plane as a function of frequency for each input port.

The realized peak gain in the azimuth plane (after compensating for the additional feed line length and the connector's insertion loss) and the SLL as a function of frequency are plotted in Figs. 16 and 17, respectively. The proposed ULA with integrated Butler matrix outperforms the Wilkinson-power-divider-based corporate-fed AA proposed in [31] in terms of peak gain and steerability. Fig. 16 shows that the 4 × 4 Butler matrix with integrated 1 × 4 ULA achieves a measured (simulated) gain of 11.05 ± 1.25 dBi (10.66 ± 0.39 dBi) for the inner beams and 9.25 ± 1.5 dBi (9.15 ± 0.64 dBi) for the outer beams in the n257 band. In addition, the Butler matrix with AA is steerable in four discrete directions covering up to 120° in terms of −3-dB beamwidth. In contrast, the corporate-fed array in [31] has a fixed beam and exhibits a realized peak gain of 10.1 ± 0.7 dBi (10.5 ± 0.6 dBi).

The obtained steering angles as a function of frequency are presented in Fig. 18. In the n257 band, the measured (simulated) main beam deviation stays within ±2.5° (±3.5°) for

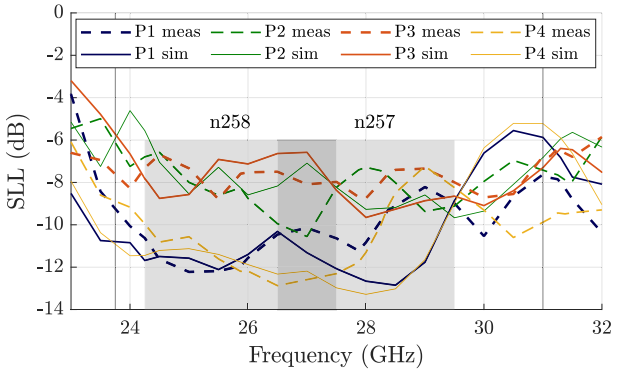

Fig. 17. Measured (dashed) and simulated (solid) SLLs as a function of frequency for each input port.

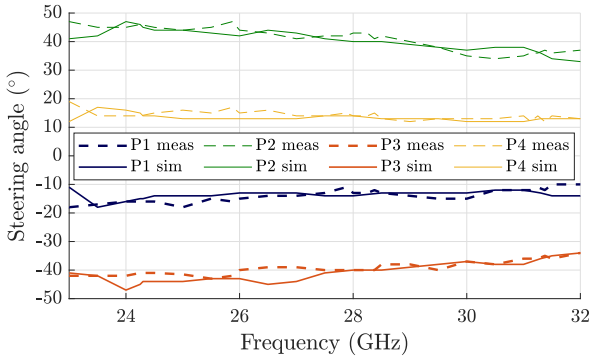

Fig. 18. Measured (dashed) and simulated (solid) beamsteering angles as a function of frequency for each input port.

all port excitations. In case of the n258 band, these deviations remain smaller than ±3° (±2.5°). Simulated and measured radiation patterns are compared in Fig. 19, while the most important far-field metrics are summarized in Table IV. Excellent agreement can be seen between simulated and measured radiation patterns. It shows reliable broadband behavior for the developed Butler matrix with integrated 1 × 4 highly efficient ULA for the targeted 5G bands.

VI. State-of-the-Art Comparison

This section compares the proposed GCPW-based 4 × 4 Butler matrix with integrated 1 × 4 highly efficient AFSIW cavity-backed patch AA to the state of the art, readily summarized in Table I.

A 4 × 4 SIW Butler matrix is integrated with a 2 × 4 ULA of slotted waveguide antennas in [12], whereas an enhanced implementation is described in [13]. Similar gain is achieved in [12], [13] despite the use of a lower loss, high-frequency laminate, and the deployment of more radiating elements while exhibiting a larger footprint. Zhong *et al.* [14] proposed an 8 × 8 SIW Butler matrix integrated with a 2 × 8 slot array. The multilayer topology halves the footprint of the Butler matrix, although it still remains more than four times larger than our solution and exhibits a reduced fractional bandwidth. An 8 × 8 SIW-based Butler matrix in multilayer PCB technology with a physically interchangeable slot AA layer for 1D and 2D steering is examined in [15]. The novelty of this design comes at the cost of moderate gain

TABLE IV

OVERALL MEASURED PERFORMANCE OF THE 4 × 4 BUTLER MATRIX (BM) WITH INTEGRATED 1 × 4 AA

BM+AA*	24.25 GHz				25.5 GHz				26.5 GHz				28 GHz				29.5 GHz				31 GHz			
	P1	P2	P3	P4	P1	P2	P3	P4	P1	P2	P3	P4	P1	P2	P3	P4	P1	P2	P3	P4	P1	P2	P3	P4
θ (°)	-16	46	-41	14	-15	45	-43	15	-14	43	-39	16	-13	43	-40	14	-15	38	-40	13	-12	36	-36	14
HPBW (°)	23	28	32	28	24	30	27	23	26	26	29	25	22	29	25	23	20	27	28	23	22	22	23	21
RG (dBi)	9.2	6.6	7	8.4	9.5	8.4	8.3	9.2	10	8.9	7.8	9.9	11.9	9.2	10.1	11.4	11	9.6	10.1	10.8	10.1	9.3	9.3	9.9
SLL (dB)	-10.6	-6.1	-6.7	-10	-12.2	-7.9	-8.1	-11.6	-10.5	-9.3	-6.8	-12.9	-10.8	-6.6	-8	-11.3	-9	-8.4	-7.3	-8.3	-7.6	-7.4	-6.8	-9.9

* θ = main beam direction, HPBW = half-power beamwidth, RG = realized peak gain, SLL = side lobe level, PX = port x.

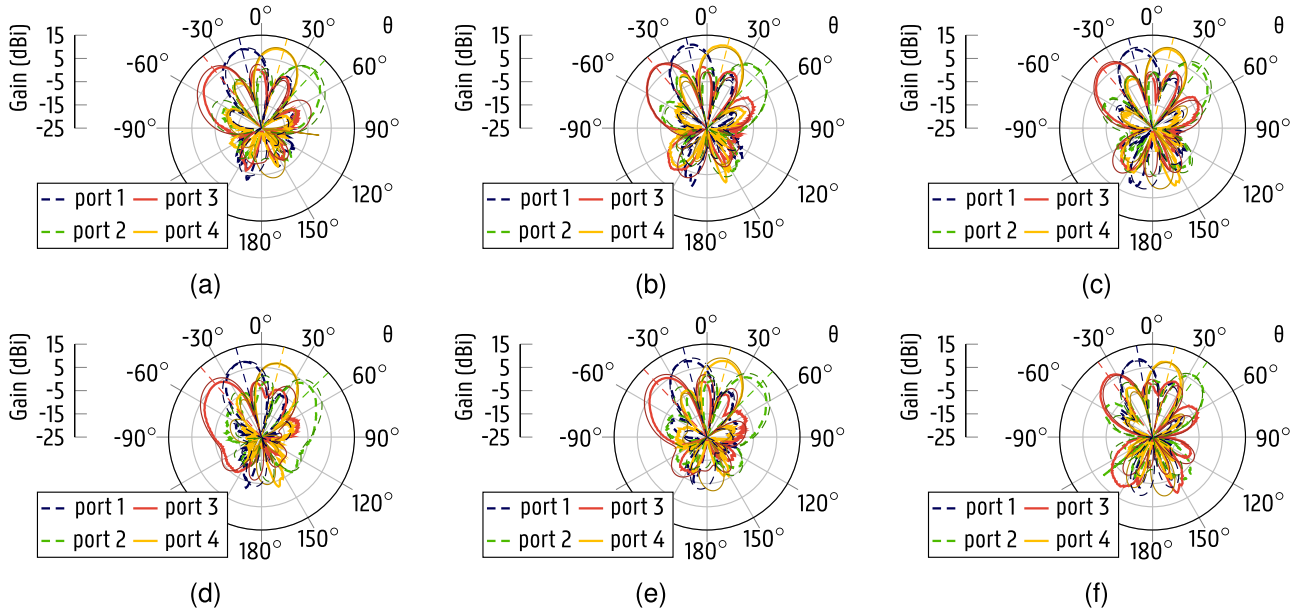

Fig. 19. Measured (thick) and simulated (thin) radiation patterns at (a) 26.5 GHz, (b) 28 GHz, (c) 29.5 GHz, (d) 24.25 GHz, (e) 25.5 GHz, and (f) 31 GHz.

and bandwidth while exhibiting a significant footprint. Integration of a dual-polarized AA onto a 4 × 4 Butler matrix, demonstrated in [16], shows excellent performance but only within a narrow scan range. In [17], a 2D scanning 9 × 9 SIW-fed Butler matrix with 3 × 3 slot array is presented. This solution makes use of a three-way coupler to maintain a reasonable footprint. Despite the larger number of antenna elements, the realized peak gain is in the same order as our proposed design and the fractional bandwidth is limited. In [18], a 2 × 2 highly efficient cavity-backed patch AA is fed by a 4 × 4 SIW Butler matrix, integrated behind the antenna elements in a multilayer PCB. While this design has a similar performance, its footprint is more than twice as large. A 16 × 16 SIW Butler matrix is connected to a 4 × 4 patch AA in [19]. An effort to reduce the footprint is attempted by employing a novel eight-way crossover and an eight-port hybrid coupler. The measured excess insertion loss of 6 dB and the amplitude imbalance of 7 dB are not negligible. Moreover, the design has a measured total efficiency of 24% and a realized maximal gain of 12.1 dBi, despite using 16 radiating elements. In conclusion, the main drawbacks of all presented SIW implementations [12]–[19] are their inherently larger footprint, the narrower bandwidth (except for [18]), and the more complicated integration process of ICs.

Next, several MSL-based designs are discussed. In [21], a 4 × 6 Butler matrix is presented, by utilizing two Wilkinson power dividers at the two outermost ports. It yields an increased simulated maximal amplitude imbalance of 5 dB and a limited fractional bandwidth of only 3.6%. A 4 × 4 patch AA with underlying 8 × 8 Butler matrix, equipped with a power divider at each output port, is implemented in [22]. The authors attribute the excess insertion loss around 4 dB and the low efficiency between 29% and 36% to the MSL technology. Single-layer PCB implementations of 4 × 4 MSL Butler matrices integrated with a 1 × 4 patch array are investigated in [23] and [24]. The former uses an aluminum enclosure to suppress undesired radiation originating from the beamforming network. The design integrates a single-pole four-throw (SP4T) switch to enable beam selection without multibeam functionality. The latter work compares three MSL-based 4 × 4 Butler matrices, all exhibiting more loss than our proposed GCPW-based solution. The 1 × 4 planar inverted-E antenna (PIEA) array with integrated Butler matrix in [25] shows reliable performance at lower frequencies, albeit with significant sidelobes. In general, we can conclude that all MSL implementations [21]–[25] suffer from undesired radiation, an increased transmission loss, a lower total efficiency, and no coverage of all global 26- and 28-GHz 5G bands.

A compact CPW-fed inverted slotline Butler matrix solution on a high permittivity laminate ($\varepsilon_r = 10.2$) for easy integration with GaAs solid-state active components is proposed in [26].

In [27], a very compact, broadband, planar Butler matrix in SL technology is demonstrated, without array integration. Both [26] and [27] operate at lower frequencies. Another compact implementation based on suspended integrated SL (SISL) technology is presented in [28]. The 4 × 4 Butler matrix is implemented in a multilayer PCB stack, which also contains the 2 × 4 patch AA. Despite their eight-antenna-element configuration, the realized maximal gain (11 dBi) is lower than in our proposed design with only four radiating elements.

A stereolithographically (SLA) 3D-printed and copper-plated 2 × 4 groove gap waveguide (GGW) Butler matrix without AA is proposed in [29]. This very narrowband air-filled implementation allows low excess insertion loss at the cost of a large footprint. Another narrowband air-filled implementation based on CNC machining of rectangular waveguides (RWGs) is presented in [30]. The achieved insertion loss and amplitude imbalance quickly deteriorate when moving away from the center frequency. The compact footprint is achieved by arranging the 4 × 4 Butler matrix in a 2 × 2 input and a 2 × 2 output configuration.

VII. Conclusion

An elaborate investigation of three novel planar GCPW quadrature hybrid couplers and two novel GCPW crossover designs yielded the optimal components for a compact, broadband and efficient Butler matrix. Their measured (excess) insertion loss remains below 0.75 and 0.5 dB while the amplitude imbalance does not exceed 0.5 and 0.2 dB for the bent hybrid coupler and multilayer crossover, respectively. In the future, an alternative high-frequency laminate with a lower loss tangent, a lower surface roughness, and an alternative surface finish may be used to mitigate transmission loss even further. Based on these building blocks and four phase shifters, a 4 × 4 Butler matrix is realized in the GCPW technology. In-depth characterization showcases a good insertion loss (<3.8 dB) and amplitude imbalance (±1.1 dB) over the entire targeted [23.75, 31] GHz band. Next, the GCPW-based Butler matrix is compactly integrated with a broadband and highly efficient 1 × 4 air-filled SIW cavity-backed patch AA. The proposed Butler matrix with ULA features a peak gain of 12.3 dBi, SLLs below −7 dB, a −3-dB beamwidth coverage of 110° in the azimuth plane, and a fractional bandwidth larger than 25%, which is sufficient to cover all global 26- and 28-GHz frequency bands. Moreover, the design fits within a small footprint of $[2\lambda_0 \times 4.3\lambda_0 \times 0.2\lambda_0]$, which makes it suitable for compact, broadband and cost-effective beamforming applications for future (5G and beyond) generation communication systems.

References

[1] J. Navarro-Ortiz, P. Romero-Diaz, S. Sendra, P. Ameigeiras, J. J. Ramos-Munoz, and J. M. Lopez-Soler, "A survey on 5G usage scenarios and traffic models," *IEEE Commun. Surveys Tuts.*, vol. 22, no. 2, pp. 905–929, 2nd Quart., 2020.

[2] M. Agiwal, H. Kwon, S. Park, and H. Jin, "A survey on 4G–5G dual connectivity: Road to 5G implementation," *IEEE Access*, vol. 9, pp. 16193–16210, 2021.

[3] K. Kibaroglu, M. Sayginer, T. Phelps, and G. M. Rebeiz, "A 64-element 28-GHz phased-array transceiver with 52-dBm EIRP and 8–12-Gb/s 5G link at 300 meters without any calibration," *IEEE Trans. Microw. Theory Techn.*, vol. 66, no. 12, pp. 5796–5811, Dec. 2018.

[4] K. Wu, H. Zhang, Y. Chen, Q. Luo, and K. Xu, "All-silicon microdisplay using efficient hot-carrier electroluminescence in standard 0.18 μm CMOS technology," *IEEE Electron Device Lett.*, vol. 42, no. 4, pp. 541–544, Apr. 2021.

[5] J. Butler and R. Lowe, "Beam-forming matrix simplifies design of electronically scanned antennas," *Electron. Des.*, vol. 9, pp. 170–173, Apr. 1961.

[6] R. J. Mailloux, *Phased Array Antenna Handbook*. Norwood, MA, USA: Artech House, 2017.

[7] N. J. G. Fonseca, "Printed S-band 4 × 4 Nolen matrix for multiple beam antenna applications," *IEEE Trans. Antennas Propag.*, vol. 57, no. 6, pp. 1673–1678, Jun. 2009.

[8] T. Djerafi, N. J. Fonseca, and K. Wu, "Broadband substrate integrated waveguide 4×4 Nolen matrix based on coupler delay compensation," *IEEE Trans. Microw. Theory Techn.*, vol. 59, no. 7, pp. 1740–1745, Jul. 2011.

[9] A. K. Vallappil, M. K. A. Rahim, B. A. Khawaja, N. A. Murad, and M. G. Mustapha, "Butler matrix based beamforming networks for phased array antenna systems: A comprehensive review and future directions for 5G applications," *IEEE Access*, vol. 9, pp. 3970–3987, 2021.

[10] L. Shevada, H. D. Raut, R. Malekar, and S. Kumar, "Comparative study of different beamforming techniques for 5G: A review," *Inventive Commun. Comput. Technol.*, vol. 145, pp. 589–595, Jan. 2021.

[11] J. Deng, O. Tirkkonen, and C. Studer, "MmWave multiuser MIMO precoding with fixed subarrays and quantized phase shifters," *IEEE Trans. Veh. Technol.*, vol. 68, no. 11, pp. 11132–11145, Nov. 2019.

[12] Q.-L. Yang, Y.-L. Ban, J.-W. Lian, Z.-F. Yu, and B. Wu, "SIW Butler matrix with modified hybrid coupler for slot antenna array," *IEEE Access*, vol. 4, pp. 9561–9569, 2016.

[13] Q. L. Yang, Y. L. Ban, K. Kang, C. Y. D. Sim, and G. Wu, "SIW multi-beam array for 5G mobile devices," *IEEE Access*, vol. 4, pp. 2788–2796, 2016.

[14] L. H. Zhong, Y. L. Ban, J. W. Lian, Q. L. Yang, J. Guo, and Z. F. Yu, "Miniaturized SIW multibeam antenna array fed by dual-layer 8×8 Butler matrix," *IEEE Antennas Wireless Propag. Lett.*, vol. 16, pp. 3018–3021, 2017.

[15] C. Bartlett and J. Bornemann, "Cross-configuration substrate integrated waveguide beamforming network for 1D and 2D beam patterns," *IEEE Access*, vol. 7, pp. 151827–151835, 2019.

[16] Q. Wu, J. Hirokawa, J. Yin, C. Yu, H. Wang, and W. Hong, "Millimeter-Wave multibeam endfire dual-circularly polarized antenna array for 5G wireless applications," *IEEE Trans. Antennas Propag.*, vol. 66, no. 9, pp. 4930–4935, Sep. 2018.

[17] J.-W. Lian, Y.-L. Ban, J.-Q. Zhu, K. Kang, and Z. Nie, "Compact 2-D scanning multibeam array utilizing the SIW three-way couplers at 28 GHz," *IEEE Antennas Wireless Propag. Lett.*, vol. 17, no. 10, pp. 1915–1919, Oct. 2018.

[18] I. Mohamed and A.-R. Sebak, "60 GHz 2-D scanning multibeam cavity-backed patch array fed by compact SIW beamforming network for 5G applications," *IEEE Trans. Antennas Propag.*, vol. 67, no. 4, pp. 2320–2331, Apr. 2019.

[19] J.-W. Lian, Y.-L. Ban, H. Zhu, and Y. J. Guo, "Uniplanar beam-forming network employing eight-port hybrid couplers and crossovers for 2-D multibeam array antennas," *IEEE Trans. Microw. Theory Techn.*, vol. 68, no. 11, pp. 4706–4718, Nov. 2020.

[20] K. Wu, M. Bozzi, and N. J. G. Fonseca, "Substrate integrated transmission lines: Review and applications," *IEEE J. Microw.*, vol. 1, no. 1, pp. 345–363, Jan. 2021.

[21] M. Ansari, H. Zhu, N. Shariati, and Y. J. Guo, "Compact planar beam-forming array with endfire radiating elements for 5G applications," *IEEE Trans. Antennas Propag.*, vol. 67, no. 11, pp. 6859–6869, Nov. 2019.

[22] K. Klionovski, M. S. Sharawi, and A. Shamim, "A dual-polarization-switched beam patch antenna array for millimeter-wave applications," *IEEE Trans. Antennas Propag.*, vol. 67, no. 5, pp. 3510–3515, May 2019.

[23] S. Lee, Y. Lee, and H. Shin, "A 28-GHz switched-beam antenna with integrated Butler matrix and switch for 5G applications," *Sensors*, vol. 21, no. 15, p. 5128, Jul. 2021.

[24] F. Pizarro, D. Ramírez-Gil, A. Algaba-Brazález, L. F. Herrán-Ontanón, and E. Rajo-Iglesias, "Comparison study of 4×4 Butler matrices in microstrip technologies for Ka-band," *Int. J. Electron. Commun.*, vol. 122, Jul. 2020, Art. no. 153248, doi: 10.1016/j.aeue.2020.153248.

[25] M. K. Ishfaq *et al.*, "Compact wide-angle scanning multibeam antenna array for V2X communications," *IEEE Antennas Wireless Propag. Lett.*, vol. 20, no. 11, pp. 2141–2145, Nov. 2021.

[26] M. Nedil, T. A. Denidni, and L. Talbi, "Novel Butler matrix using CPW multilayer technology," *IEEE Trans. Microw. Theory Techn.*, vol. 54, no. 1, pp. 499–507, Jan. 2006.

[27] K. Wincza, S. Gruszczynski, and K. Sachse, "Broadband planar fully integrated 8×8 Butler matrix using coupled-line directional couplers," *IEEE Trans. Microw. Theory Techn.*, vol. 59, no. 10, pp. 2441–2446, Oct. 2011.

[28] Y. Wang, K. Ma, and Z. Jian, "A low-loss Butler matrix using patch element and honeycomb concept on SISL platform," *IEEE Trans. Microw. Theory Techn.*, vol. 66, no. 8, pp. 3622–3631, Aug. 2018.

[29] A. Tamayo-Domínguez, J. Fernández-González, and M. Sierra-Castañer, "3-D-printed modified Butler matrix based on gap waveguide at W-band for monopulse radar," *IEEE Trans. Microw. Theory Techn.*, vol. 68, no. 3, pp. 926–938, Mar. 2020.

[30] D.-H. Kim, J. Hirokawa, and M. Ando, "Design of waveguide short-slot two-plane couplers for one-body 2-D beam-switching Butler matrix application," *IEEE Trans. Microw. Theory Techn.*, vol. 64, no. 3, pp. 776–784, Mar. 2016.

[31] I. Lima de Paula *et al.*, "Cost-effective high-performance air-filled SIW antenna array for the global 5G 26 GHz and 28 GHz bands," *IEEE Antennas Wireless Propag. Lett.*, vol. 20, no. 2, pp. 194–198, Feb. 2021.

[32] L. Van Messem *et al.*, "Substrate integrated components for passive millimeterwave-frequency beamforming networks," in *IEEE MTT-S Int. Microw. Symp. Dig.*, Nov. 2021, pp. 272–274.

[33] A. B. Guntupalli, T. Djerafi, and K. Wu, "Two-dimensional scanning antenna array driven by integrated waveguide phase shifter," *IEEE Trans. Antennas Propag.*, vol. 62, no. 3, pp. 1117–1124, Mar. 2014.

[34] A. A. Abdulbari, S. K. A. Rahim, P. J. Soh, M. H. Dahri, A. A. Eteng, and M. Y. Zeain, "A review of hybrid couplers: State-of-the-art, applications, design issues and challenges," *Int. J. Numer. Model., Electron. Netw., Devices Fields*, vol. 34, no. 5, pp. 1–19, Jun. 2021.

[35] L. Bogaert *et al.*, "A 5-bit, 1.6ps resolution true time delay optical beamforming network for 4-element antenna arrays," in *Proc. Int. Topical Meeting Microw. Photon. (MWP)*, Nov. 2021, pp. 5–8.

[36] K. Xu, "Silicon electro-optic micro-modulator fabricated in standard CMOS technology as components for all silicon monolithic integrated optoelectronic systems," *J. Micromech. Microeng.*, vol. 31, no. 5, Apr. 2021, Art. no. 054001.

[37] D. M. Pozar, *Microwave Engineering*. Hoboken, NJ, USA: Wiley, 2011.

[38] L. Chiu and Q. Xue, "Investigation of a wideband 90° hybrid coupler with an arbitrary coupling level," *IEEE Trans. Microw. Theory Techn.*, vol. 58, no. 4, pp. 1022–1029, Apr. 2010.

[39] M. Bozzi, A. Georgiadis, and K. Wu, "Review of substrate-integrated waveguide circuits and antennas," *IET Microw., Antennas Propag.*, vol. 5, no. 8, p. 909, 2011. [Online]. Available: http://digital-library.theiet.org/content/journals/10.1049/iet-map.2010.0463

[40] A. A. M. Ali, N. J. G. Fonseca, F. Coccetti, and H. Aubert, "Design and implementation of two-layer compact wideband Butler matrices in SIW technology for Ku-band applications," *IEEE Trans. Antennas Propag.*, vol. 59, no. 2, pp. 503–512, Feb. 2011.

[41] G. Gold and K. Helmreich, "A physical surface roughness model and its applications," *IEEE Trans. Microw. Theory Techn.*, vol. 65, no. 10, pp. 3720–3732, Oct. 2017.

[42] Y. Tao and F. Scharf, "Revisiting the effect of nickel characteristics on high-speed interconnect performance," *IEEE Trans. Microw. Theory Techn.*, vol. 64, no. 8, pp. 2447–2453, Aug. 2016.

Laura Van Messem (Student Member, IEEE) received the M.Sc. degree in electrical engineering from Ghent University, Ghent, Belgium, in 2019. She is currently pursuing the Ph.D. degree in electrical engineering at the IDLab-Electromagnetics Group, Department of Information Technology (INTEC), Ghent University/imec.

Her research interests include next-generation communication systems, more specifically highly efficient millimeterwave and THz passive solutions.

Arno Moerman (Student Member, IEEE) received the M.Sc. degree from Ghent University, Ghent, Belgium, in 2019.

He is currently a Ph.D. Researcher with Ghent University/imec. His research interest includes antenna systems for future generation mobile communication networks.

Olivier Caytan (Member, IEEE) received the M.Sc. and Ph.D. degrees in electrical engineering from Ghent University, Ghent, Belgium, in 2014 and 2019, respectively.

He is currently a Post-Doctoral Researcher with the Electromagnetics Group, Department of Information Technology, Ghent University/imec. His research interests include microwave engineering and active antenna systems, in particular mm-wave opto-electronic antenna systems for 5G and beyond.

Igor Lima de Paula received the B.Sc. degree in electrical engineering from the Federal University of Juiz de Fora, Juiz de Fora, Brazil, in 2015, and the M.Sc. degree from Ghent University, Ghent, Belgium, in 2018.

He is currently a Ph.D. Researcher with the IDLab-Electromagnetics Group, Department of Information Technology (INTEC), Ghent University/imec. His research interests include antenna integration in the context of the Internet of Things and the design of multi-antenna systems with microwave photonic devices for radio-over-fiber applications in future mobile communication networks.

Bram Hoflack is currently pursuing the M.Sc. degree in electrical engineering: electronic circuits and systems at Ghent University, Ghent, Belgium.

Bram Stroobandt received the B.Sc. degree in electrical engineering from Ghent University, Ghent, Belgium, in 2020, where he is currently pursuing the M.Sc. degree in electrical engineering: communication and information technology.

Sam Lemey (Member, IEEE) received the M.Sc. degree in electronic engineering from Howest, University College West Flanders, Kortrijk, Belgium, in 2012, and the Ph.D. degree in electrical engineering from Ghent University, Ghent, Belgium, in 2016.

From January to March 2018, he was a Visiting Scientist with the Terahertz Photonics Group, Institute of Electronics, Microelectronics and Nanotechnology (IEMN), University Lille Nord de France, Lille, France. He is currently an Assistant Professor with the Department of Information Technology (INTEC), Ghent University/imec. His research interests include antenna systems for wearable applications, active antenna design for the Internet of Things and (beyond) 5G applications, (opto-electronic) millimeter-wave multi-antenna systems, impulse-radio ultra-wideband antenna systems for centimeter-precision localization, and full-wave/circuit co-optimization frameworks to realize (opto-electronic) active (multi-)antenna systems.

Dr. Lemey received the International Union of Radio Science (URSI) Young Scientist Award at the 2020 URSI General Assembly and the Best Paper Award at the 2016 IEEE MTT-S Topical Conference on Wireless Sensors and Sensor Networks. He was a co-recipient of the 2015 Best Paper Award at the 22nd IEEE Symposium on Communications and Vehicular Technology in the Benelux and the 2019 European Conference on Optical Communication Best Demo Award.

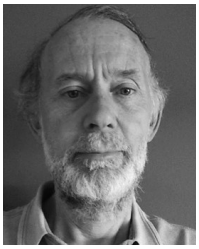

Marc Moeneclaey (Fellow, IEEE) received the Diploma and Ph.D. degrees in electrical engineering from Ghent University, Ghent, Belgium, in 1978 and 1983, respectively.

He is currently a Professor with the Department of Telecommunications and Information Processing (TELIN), Ghent University. He is the author of more than 500 scientific articles in international journals and conference proceedings. Together with Prof. H. Meyr (RWTH Aachen, Aachen, Germany) and Dr. S. Fechtel (Siemens AG, München, Germany), he has coauthored the book *Digital Communication Receivers—Synchronization, Channel Estimation, and Signal Processing* (Wiley, 1998). His main research interests include statistical communication theory, carrier and symbol synchronization, bandwidth-efficient modulation and coding, spread spectrum, and satellite and mobile communication.

Dr. Moeneclaey was a co-recipient of the Mannesmann Innovations Prize 2000. From 1992 to 1994, he was an Editor for Synchronization of the IEEE TRANSACTIONS ON COMMUNICATIONS. He has served as a Co-Guest Editor for Special Issues of the *Wireless Personal Communications* journal (on Equalization and Synchronization in Wireless Communications) in 1998 and the IEEE JOURNAL ON SELECTED AREAS IN COMMUNICATIONS (on Signal Synchronization in Digital Transmission Systems) in 2001.

Hendrik Rogier (Senior Member, IEEE) received the electrical engineering and Ph.D. degrees from Ghent University, Ghent, Belgium, in 1994 and 1999, respectively.

From October 2003 to April 2004, he was a Visiting Scientist with the Mobile Communications Group, Vienna University of Technology, Vienna, Austria. He is currently a Senior Full Professor with the Department of Information Technology, Ghent University, and a Guest Professor with the Interuniversity Microelectronics Centre, Ghent. He authored or coauthored about 180 articles in international journals and about 200 contributions in conference proceedings. His current research interests include antenna systems, radiowave propagation, body-centric communication, numerical electromagnetics, electromagnetic compatibility, and power/signal integrity.

Dr. Rogier was twice awarded the URSI Young Scientist Award. He received the 2014 Premium Award for Best Paper in *IET Electronics Letters* and several awards at conferences. He is an Associate Editor of the *IET Electronics Letters* and the *IET Microwaves, Antennas and Propagation*. He acts as the URSI Commission B representative for Belgium.